Nuclear Instruments and Methods in Physics Research B 394 (2017) 1–5

Contents lists available at ScienceDirect

Nuclear Instruments and Methods in Physics Research B

journal homepage: www.elsevier.com/locate/nimb

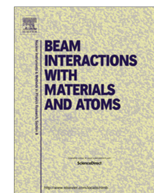


# High aspect ratio channels in glass and porous silicon

H.D. Liang [a,b], Z.Y. Dang [a], J.F. Wu [a,c], J.A. van Kan [a], S. Qureshi [a], M.D. Ynsa [d,e], V. Torres-Costa [d,e], A. Maira [d], T.V. Venkatesan [b], M.B.H. Breese [a,*]

[a] Centre for Ion Beam Applications (CIBA), Department of Physics, National University of Singapore, Singapore 117542
[b] Nanoscience and Nanotechnology Initiative (NNI), National University of Singapore, Singapore 117411
[c] Department of Electrical and Computer Engineering, National University of Singapore, Singapore 117583
[d] Department of Applied Physics, Universidad Autónoma de Madrid, Madrid, Campus de Cantoblanco, 28049 Madrid, Spain
[e] Centro de Micro-Análisis de Materiales (CMAM), Universidad Autónoma de Madrid, Campus de Cantoblanco Edif. 22, Faraday 3, E-28049 Madrid, Spain

ARTICLE INFO

*Article history:*
Received 18 October 2016
Accepted 12 December 2016

*Keywords:*
Proton beam irradiation
High-aspect-ratio channel
Porous silicon

ABSTRACT

We have developed a micromachining process to produce high-aspect-ratio channels and holes in glass and porous silicon. Our process utilizes MeV proton beam irradiation of silicon using direct writing with a focused beam, followed by electrochemical etching. To increase throughput we have also developed another process for large area ion irradiation based on a radiation-resistant gold surface mask, allowing many square inches to be patterned. We present a study of the achievable channel width, depth and period and sidewall verticality for a range of channels which can be over 100 μm deep or 100 nm wide with aspect ratios up to 80. This process overcomes the difficulty of machining glass on a micro- and nanometer scale which has limited many areas of applications in different fields such as microelectronics and microfluidics.

© 2016 Published by Elsevier B.V.

## 1. Introduction

In microfluidics studies devices made from glass have many highly-ideal properties [1–4] such as robustness and transparency, absence of swelling, re-usability and ability to withstand heat treatment, a tendency not to absorb chemicals, and good surface properties for DNA and their complexes with proteins. The problem which has limited its use is the difficulty in machining suitable glass structures. Conventional processes cannot readily form nanometer scale channels or allow integration in 3D device architectures. Other processes such as femtosecond laser patterning [5–7] and laser lithography [8] have been used to fabricate micro- and nanochannels but have limited resolution. Other fields as such as sensors also make use of porous silicon channels [9].

In microelectronics the demand for higher functionality requires new packaging strategies, such as wafer stacking [10–13]. This enables logic chips to be combined with memory chips in an economical manner. This has led to the development of thin interposers (an interposer is an insulator layer which serves as an interface which joins the input/output circuitry of the various dies and the substrate). A variety of materials have been studied for use as interposers. For example, silicon necessitates thinning by grinding, laminates have high electrical loss and are assembled in a complex suite of processes. Organics have a limited dimensional stability, lithography limitations and low thermal conductivity. The main advantage of glass as an interposer is its very good high frequency properties but other attractive properties are high mechanical stability, a thermal expansion coefficient which is similar to that of silicon, low insertion loss, high electrical resistivity, high thermal stability and optical transparency for integrated photonic chips.

One of the hurdles to the uptake of glass interposers is in fabricating high density of channels in a material which is fragile in thin layers and in large sizes. Several processes have been studied for drilling holes in glass interposers, each with different limitations for producing high aspect ratio channels, e.g. tapered hole widths, surface roughness, minimum hole size. One of the most successful recent approaches is laser ablation [11] which has produced holes of tens of microns in diameter in glass sheets of 100 μm thickness. This study also showed drilled hole diameters of 10 μm in 30 μm thick glass sheets.

## 2. Vertical channel fabrication process

We previously developed a fabrication process [14,15] for producing buried, hollow channels parallel to the surface in fully oxidized porous silicon (FOPS), which is a type of glass. This process is

* Corresponding author.
*E-mail address:* phymbhb@nus.edu.sg (M.B.H. Breese).

http://dx.doi.org/10.1016/j.nimb.2016.12.025
0168-583X/© 2016 Published by Elsevier B.V.

based on irradiation of low resistivity, 0.02 Ω.cm, p-type silicon with high energy ions. 2 MeV protons are typically used, these are focused within a nuclear microprobe [16] to a spot size which can be as small as 20 nm [17] and scanned over the surface to create a pattern of damage. 2 MeV protons penetrate the surface with little scattering, as simulations show in Fig. 1a, produced using the SRIM (Stopping and Range of Ions in Matter) code [18,19], before coming to rest at the end-of-range depth of around 50 μm. Collisions with sample atoms results in a range of defects being created [20,21]. The rate of defect generation is a maximum close to the end-of-range penetration depth where a small volume is significantly damaged, Fig. 1b, while the above region which is closer to the surface has an order of magnitude less damage. The end-of-range depth can be tuned by varying the ion energy, allowing volumes which are well-defined in position and depth to be controllably and selectively damaged. Ion irradiation introduces damage mostly as vacancy-interstitial pairs (i.e. Frenkel defects), some of which lower the concentration of free charge carriers within the irradiated silicon. For low fluence ion irradiation these end-of-range regions are only partially depleted of charge carriers, i.e. their resistivity is increased by one or two orders of magnitude to a regime where high porosity microporous silicon is formed [14,15,22] during subsequent electrochemical anodization in hydrofluoric acid (HF) solution (24% HF, from a 1:1 solution of HF (48%): ethanol). The lower resistivity, unirradiated silicon forms lower porosity mesoporous silicon.

After rinsing in ethanol and then in distilled water the sample is subjected to room temperature oxidation for several days, resulting in the highly porous regions at the end-of-range becoming fully oxidized and are selectively removed in dilute HF, while the surrounding lower porosity mesoporous silicon is largely unaffected. Such porous silicon (PSi) structures containing can be turned into oxidized porous silicon by the use of high temperature oxidation.

We have modified this process to fabricate high aspect ratio vertical channels, making use of the low defect density region which extends from the silicon surface to just above the end-of-range region, Fig. 1b. At a low fluence this region is little affected and only around the end-of-range depth is the resistivity sufficiently increased to form high porosity microporous silicon. However, for an order of magnitude higher fluence the damage close to the surface is now also sufficient to produce high porosity silicon, e.g. Fig. 1c which was created by irradiating with a 2 MeV proton fluence of $4 \times 10^{16}/cm^2$ with a focused beam spot size of 200 nm. The sample was etched to a depth of 60 μm i.e. beyond the end-of-range of 50 μm, then cleaved for cross-section imaging. Intense photoluminescence (PL) emission, corresponding to the formation of microporous silicon at the more resistive regions, is now observed from the irradiated column, Fig. 1d. The highly porous column can be removed after room temperature oxidation and immersion in HF as described above, leaving a high aspect ratio channel which runs from the surface to depths of tens of microns, Fig. 1e. At the end-of-range depth the higher fluence now results in this region being highly resistive and so not undergoing anodization, remaining as crystalline silicon. This has been used to fabricate 3D silicon micro- and nanoscale structures using the crystalline bars remaining at the end-of-range [23,24]. Depending on the required structures one may stop etching before this depth is reached. One may leave the porous layer in place or separate it for further processing as required.

Fig. 2 shows the full range of effects which occur with increasing 2 MeV proton fluence on channel creation in porous silicon along the ion trajectory. At the lowest fluence, Fig. 2a, a narrow buried channel is observed at the end-of-range depth, with higher porosity silicon above it, though not extending to the surface. For a higher fluence, Fig. 2b,c, growth of a solid core is observed at the end-of-range depth, corresponding to where the silicon is most damaged and so not undergoing etching. Above this the column of higher porosity silicon extends to the surface. For even higher fluences, Fig. 2d,e large silicon cores remain at the end-of-range depth and hollow columns above which extend to the surface. This zone comprises highly porous silicon which can be removed to form the hollow columns in Fig. 2d,e. Note the onset of vertical channel creation along the column occurs at a fluence which is one order of magnitude greater than where the onset of channel creation at the end-of-range is observed, corresponding to the order of magnitude difference in defect density.

There are various factors that influence the channel width and profile, such as fluence, etch current density, oxidation conditions. We have studied the effects of these factors for producing hollow channels at the end-of-range [15]. Channel widths generally increase with fluence, as the carrier density across a wider zone away from the beam axis becomes sufficiently lowered to produce high porosity silicon during anodization, thus the channel in Fig. 2e is wider than in Fig. 2d. Fig. 3 shows different views of channels created in porous silicon using these two fluences, respectively resulting in channel widths of 0.6 and 0.8 μm.

Thus to produce narrow channels the fluence should be as low as is consistent with complete removal of the irradiated volume; if the fluence is too low then the channel may not be fully emptied, with some low porosity flakes remaining. This is seen in Fig. 3a where small flakes within the channels close to the surface remain, these are less commonly observed in channels irradiated with a higher fluence where the higher porosity allows more efficient removal of the irradiated volume. In Fig. 3b,c one observes the very high verticality of the etched channels to a depth of 40 μm, under optimal irradiation and etching conditions. Since a 2 MeV proton beam is not significantly scattered in passing through this depth then aspect ratios of 50 to 80 are achieved with smooth channel

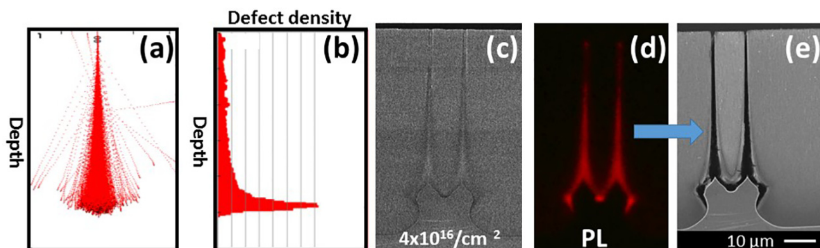


**Fig. 1.** (a), (b) Simulated plots using SRIM for 2 MeV protons in silicon respectively showing the trajectories and defect distribution versus depth. In (a) the box size is 30 μm (horizontal) × 60 μm (vertical). (c) Cross-section SEM created by irradiating two lines with a separation of 10 μm and a 2 MeV proton fluence of $4 \times 10^{16}/cm^2$, then etched at a current density of 100 mA/cm$^2$. Before PSi removal. (d) PL image of the same area showing intense emission along the irradiated track. (e) Cross-section SEM of the same area after PSi removal.

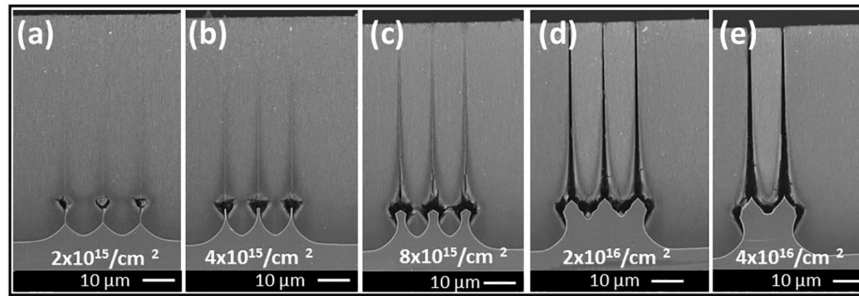


**Fig. 2.** Cross-section SEMs showing the effect of different 2 MeV proton fluences of (a) $2 \times 10^{15}/cm^2$, (b) $4 \times 10^{15}/cm^2$, (c) $8 \times 10^{15}/cm^2$, (d) $2 \times 10^{16}/cm^2$, (e) $4 \times 10^{16}/cm^2$. These channels were created by irradiating two or three lines with a separation of 10 µm. The sample was etched to a depth of 60 µm at a current density of 100 mA/$cm^2$ and the high porosity PSi removed.

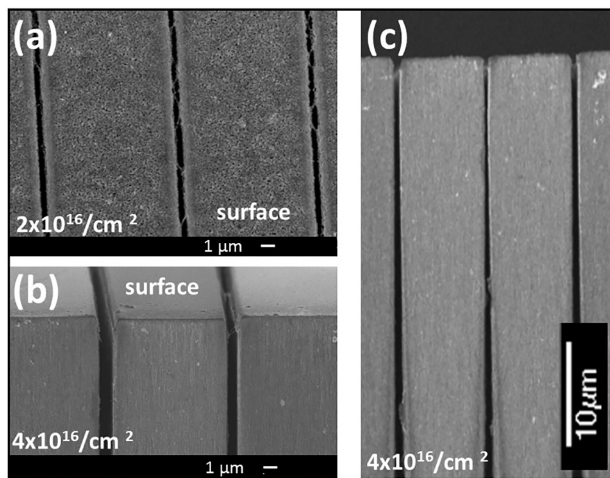


**Fig. 3.** SEMs showing different views of the two highest fluence irradiations of 2 and $4 \times 10^{16}/cm^2$ in Fig. 2, showing (a) the surface in plan-view, (b) tilted to show the surface and upper part of the etched depth, (c) top 40 µm cross-section showing the very high verticality of the etched channel.

profiles. Since a focused proton beam is used for direct writing over the silicon surface then vertical channels can be created in any desired shape; Fig. 4 shows square and circular holes 2 µm wide.

For many applications in microfluidics it is not necessary to produce such channels through thickness of tens of microns, a few microns is sufficient. Here a lower proton beam energy, e.g. 1 MeV with a range of 15 µm, may be more appropriate, furthermore it is easier to produce on a wider range of accelerators and easier to focus as the required quadrupole lens strengths are lower [17] and so stability of the system for writing is easier to achieve. For other applications, e.g. in interposers for microelectronic chip packages, channel depths of 100 µm may be required. Here a higher proton beam energy, e.g. 4 MeV protons have a range of 150 µm, is more appropriate. We have studied channel creation for both 1 MeV and for 4 MeV protons in order to demonstrate the wide applicability of this process.

The simulated lateral scattering of 1 and 2 MeV protons is compared in Fig. 5a; lower energies tend to exhibit more lateral scattering and beyond a depth of a few microns the beam width starts to increase. Fig. 5b,c show channels produced using a 1 MeV proton beam focused to a spot size of ~50 nm. Under optimal fluence and etching current density, channel widths of 100 nm are produced at the surface, Fig. 5b. Under the same conditions the cross-section views in Fig. 5c show that while the channel width increase significantly beyond a depth of 10 µm, for etch depths of 5 µm then high resolution patterning with a channel width of 150 nm is achievable with almost no broadening, giving an aspect ratio of more than 30.

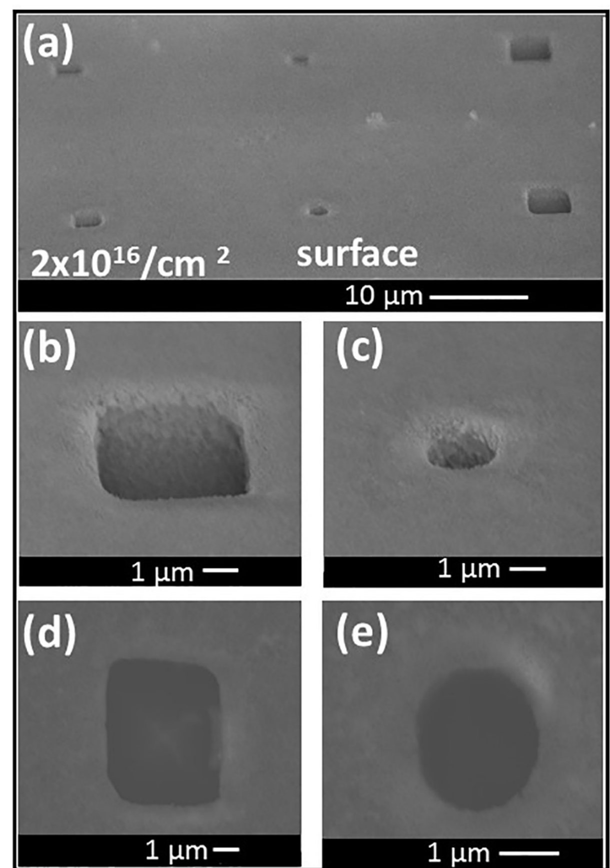


**Fig. 4.** Plan view SEMs of the surface for a 2 MeV proton fluence of $2 \times 10^{16}/cm^2$ showing square and circular hole geometries, with the PSi removed.

Fig. 6 shows results of long lines and circular channels fabricated using 4 MeV protons, where the high penetration depth enables deep channels to be fabricated. Since this energy is above the threshold for neutron production, we used remote-operation of microprobe under computer control, available at CMAM, Madrid [25]. Fig. 6a shows millimeter-long lines and Fig. 6b show 10 µm diameter holes with a 30 µm period. Fig. 6c shows a cross-section SEM of long lines similar to those in Fig. 6a in which channels over 100 µm deep are produced with little broadening along their length. Note that in Fig. 6c the etch current density was reduced so that the resulting PSi was sufficiently robust to prepare a cross-section sample for imaging, leading to the channels not being completely empty.

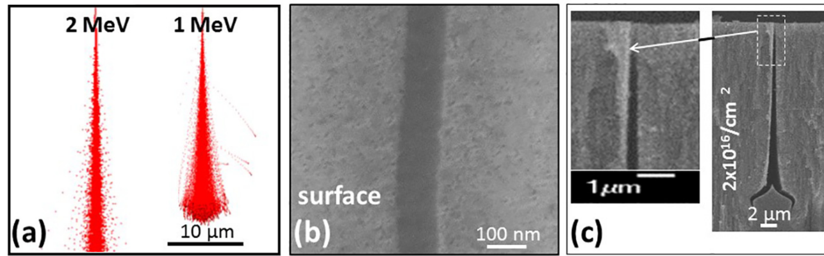


**Fig. 5.** (a) SRIM simulations of the trajectories of (left) 2 MeV and (right) 1 MeV protons in silicon. The box size is 20 μm × 20 μm. (b) plan view SEM of a 100 nm wide channel with a 1 MeV proton fluence of $2 \times 10^{16}/cm^2$. (c) Cross-section SEMs of similar channel as in (b), showing (right) the full anodized depth beyond the end-of-range at 15 μm and (left) the top 5 μm where a channel width of 150 nm is produced.

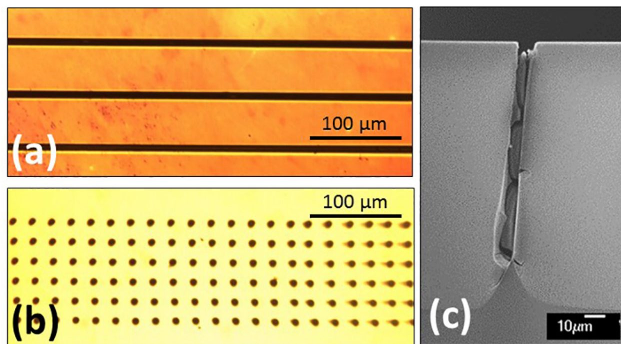


**Fig. 6.** (a), (b) optical micrographs of lines and holes fabricated using a 4 MeV proton fluence of $4 \times 10^{16}/cm^2$, etched to a depth of 100 μm. (c) Cross-section SEM of long lines similar to those shown in (a).

## 3. Large area irradiation through gold masks

Some other issues remain before this process can be routinely and reliably used for producing suitable patterned areas of porous silicon or glass. The above method for high-energy ion irradiation is based on direct-writing with a focused proton MeV beam in a nuclear microprobe, ideal for studying the basic science and optimizing conditions of a process with different fluences. However, it has the same limitations as all direct-write processes, namely it is slow and can only pattern limited areas. To get around this we constructed an irradiation facility based on the CIBA megavolt accelerator and microprobe which is used to project a divergent MeV ion beam over a large wafer area, suitable for patterning wafers to depths of several tens of micrometers [26]. Up to 1 microAmp of beam current can be delivered for irradiation with this facility, allowing to irradiate areas of 1 in. square in a matter of minutes. This facility opened up many applications to produce large-area patterned structures for use in photonics and microfluidics.

We have used this large area irradiation facility with proton beam energies of one hundred keV, with a range of less than 1 μm in polymer and silicon. A PMMA (poly(methyl methacrylate)) resist layer is deposited on the wafers surface and patterned using standard photolithography or e-beam lithography. The PMMA is thicker than the ion range so only the exposed wafer portions are irradiated. For our initial range of applications a low proton fluence ($\sim 10^{14}/cm^2$) was sufficient to make silicon stencils and other 3D structures. However, for the glass machining described in the paper, higher fluences of $>10^{16}$ protons/cm$^2$ are required and polymer masks suffer severe degradation and beam heating issues under these conditions. We have therefore developed the use of gold as the surface mask. Gold is a radiation-hard material and it is easy to electroplate to thicknesses of many microns. It conducts heat excellently, making it an ideal masking material for high fluence, high current irradiations. Furthermore, owing to its high density the gold mask needs to be typically only one third of the ion range in silicon.

Fig. 7a shows how gold surface patterns of thickness ~20 μm are used for large area patterned irradiation using 2 MeV protons, which have a range of about one third in gold (range ~15 μm) compared to silicon (range ~50 μm). After forming the inverse pattern in a thick polymer layer, gold is electroplated to the required thickness of 20 μm in this case with suitable hole sizes and periods, Fig. 7b. An important requirement is to grow the gold layer thicker than the ion range as it tends to exhibit a rough surface with a thickness varying from point to point. Fig. 7c shows channels created using a large area 2 MeV proton beam fluence of $4 \times 10^{16}/cm^2$ irradiating through such a gold mask. After anodization and PSi removal a patterned hole array is produced which can extend over full wafer areas if required.

## 4. Conclusions

Vertical channels have been produced using a new process based on proton beam irradiation and electrochemical etching. Channels may be written in the forms of narrow lines or arrays of circular or square channels with high aspect ratio. This

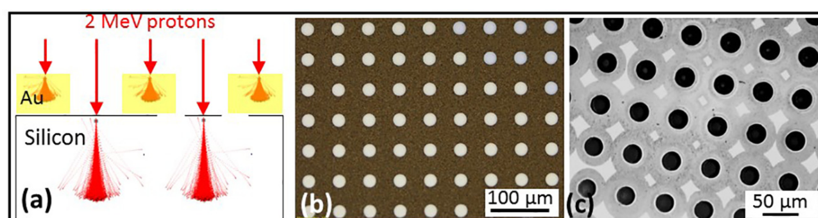


**Fig. 7.** (a) Schematic showing gold stencils used for large area patterned irradiation using high fluences of 2 MeV protons. (b) optical micrograph of gold pattern with hole diameters of 25 μm. (c) optical micrograph of large array of vertical holes fabricated in PSi using this process.

capability already far exceeds what can be achieved with other glass patterning techniques and is being applied to connecting horizontal channels in 3D arrays of microfluidic channels, and for through glass vias for interposers in microelectronics.

## Acknowledgement

This work has been partially funded by a UAM-Banco de Santander Interuniversity Cooperation with Asia Grant (2015–2016). JFW thanks the Singapore National Research Foundation (NRF) Competitive Research Programme (CRP Award No. NRF-CRP13-2014-04).

## References

[1] A. Weisberg, H.H. Bau, J.N. Zemel, Int. J. Heat Mass Transfer 35 (1992) 2465–2474.
[2] D.J. Harrison, K. Fluri, K. Seiler, Z. Fan, C.S. Effenhauser, A. Manz, Science 261 (1993) 895–897.
[3] S.C. Jacobson, R. Hergenroder, L.B. Koutny, R.J. Warmack, J.M. Ramsey, Anal. Chem. 66 (1994) 1107–1113.
[4] A.T. Woolley, R.A. Mathies, Proc. Natl. Acad. Sci. 91 (1994) 11348–11352.
[5] A.P. Esser-Kahn, P.R. Thakre, H. Dong, J.F. Patrick, V.K. Vlasko-Vlasov, N.R. Sottos, J.S. Moore, S.R. White, Adv. Mater. 23 (2011) 3654–3658.
[6] M. Masuda, K. Sugioka, Y. Cheng, N. Aoki, M. Kawachi, K. Shinoyama, K. Toyoda, H. Helvajian, K. Midorikawa, Appl. Phys. A: Mater. Sci. Proc. 76 (2003) 857–860.
[7] S. Kiyama, S. Matsuo, S. Hashimoto, Y. Morihira, J. Phys. Chem. C 113 (2009) 11560–11566.
[8] Y. Liao, Y. Cheng, C. Liu, J. Song, F. He, Y. Shen, D. Chen, Z. Xu, Z. Fan, X. Wei, K. Sugioka, K. Midorikawa, Lab. Chip 13 (2013) 1626–1631.
[9] E.H.M. Camara, C. Pijolat, J. Courbat, P. Breuil, D. Briand, N.F. de Rooij, in: IEEE Proc. Of Transducers 2007 International Solid-State Sensors, Actuators and Microsystems, (2007) 249–252.
[10] M. Töpper, I. Ndip, R. Erxleben, L. Brusberg, N. Nissen, H. Schröder, H. Yamamoto, G. Todt, H. Reichl, in: IEEE Proc. 60th Electronic Components and Technology Conference (ECTC) (2010) 66–73.
[11] R. Delmdahl, R. Paetzel, J. Microelectron. Packag. Soc. 21 (2014) 53–57.
[12] S. Takahashi, K. Horiuchi, S. Mori, K. Tatsukoshi, M. Ono, M. Mikayama, N. Imajo, T. Mobley, in: IEEE Microelectronics Packaging Conf. (EMPC) European, (2013) 1–4.
[13] Y. Sun, Y. Daquan, R. He, F. Dai, X. Sun, L. Wan, Thirteenth Int. Conf. on Electronic Packaging Technology and High Density Packaging (ICEPT-HDP), (2012) 49–51.
[14] S. Azimi, Z.Y. Dang, C. Zhang, J. Song, M.B.H. Breese, C.H. Sow, J.A. van Kan, J.R.C. van der Maarel, Lab. Chip 14 (2014) 2081–2089.
[15] Z.Y. Dang, D.Q. Liu, S. Azimi, M.B.H. Breese, RSC Adv. 4 (2014) 57402.
[16] M.B.H. Breese, G.W. Grime, F. Watt, Annu. Rev. Nucl. Part. Sci. 42 (1992) 1–38.
[17] Y. Yao, J.A. van Kan, Nucl. Instrum. Methods B 348 (2015) 203–208.
[18] J.F. Ziegler, J.P. Biersack, U. Littmark, The Stopping and Range of Ions in Solids, Pergamon Press, New York, 2003.
[19] J.F. Ziegler, M.D. Ziegler, J.P. Biersack, Nucl. Instrum. Methods B 268 (2010) 1818–1823.
[20] B.G. Svensson, C. Jagadish, A. Hallen, J. Lalita, Nucl. Instrum. Methods B 106 (1995) 183–190.
[21] A. Hallen, N. Keskitalo, F. Masszi, V. Nagl, J. Appl. Phys. 79 (1996) 3906–3914.
[22] V. Lehmann, Electrochemistry of Silicon: Instrumentation, Science, Materials and Applications, Wiley-VCH, New York, 2002.
[23] S. Azimi, M.B.H. Breese, Z.Y. Dang, Y. Yan, Y.S. Ow, A.A. Bettiol, J. Micromech. Microeng. 22 (2012) 015015.
[24] Z.Y. Dang, J. Song, S. Azimi, M.B.H. Breese, J. Forneris, E. Vittone, Nucl. Instrum. Methods B 296 (2013) 32–40.
[25] M.D. Ynsa, M.A. Ramos, N. Skukan, V. Torres-Costa, M. Jakšić, Nucl. Instrum. Methods B 348 (2015) 174–177.
[26] D. Mangaiyarkarasi, Y.S. Ow, M.B.H. Breese, V.L.S. Fuh, E.T. Xioasong, Opt. Express 16 (2008) 12757–12763.